

The mass dependence of dark matter halo alignments with large-scale structure

Davide Piras^{1,2★}, Benjamin Joachimi¹, Björn Malte Schäfer³, and more

¹*Department of Physics and Astronomy, University College London, Gower Street, London WC1E 6BT, UK*

²*Dipartimento di Fisica “G. Galilei”, Università di Padova, via Marzolo 8, I-35131 Padova, Italy*

³*Astronomisches Recheninstitut, Zentrum für Astronomie der Universität Heidelberg, Philosophenweg 12, 69120 Heidelberg, Germany*

18 May 2017

ABSTRACT

Tidal gravitational forces can modify the shape of galaxies and clusters of galaxies, thus correlating their orientation with the surrounding density field. We study the dependence of this phenomenon, known as intrinsic alignment (IA), on the mass of the dark matter haloes that host these bright structures, analysing the Millennium and Millennium-XXL N-body simulations. We closely follow the observational approach, measuring the halo position-halo shape alignment and subsequently dividing out the dependence on halo bias. We derive a theoretical scaling of the IA with mass in a dark matter Universe, and test it on simulations through a Bayesian analysis, assuming for the intrinsic alignment amplitude a power-law model with slope β_M . We find that simulation data excellently agree with the theory forecast, both yielding an estimate compatible with $\beta_M = 1/3$, and that this result does not depend on redshift or on the definition of the tensor used to describe the shape of the haloes. We repeat the analysis using observational data, obtaining a significantly higher value, namely $\beta_M \simeq 1/2$: we propose reasons to explain the discrepancy, which could be investigated with large hydrodynamical simulations.

Key words: galaxies: halos – dark matter – large-scale structure of Universe

1 INTRODUCTION

In an isotropic Universe, one would expect galaxy images not to have any preferred orientations; however, we observe that galaxy shapes are locally correlated with the surrounding large-scale structure, and therefore with each other. Several mechanisms have been proposed to explain this, such as the accretion of new material along favoured directions, and the effect of gravitational tidal fields from the surrounding dark matter haloes. In this latter picture, in particular, the aspect of luminous matter structures is shaped through tidal interactions by the hosting dark matter halo, and one can safely assume that bright and dark matter share the same shape (Kiessling et al. 2015).

This phenomenon is known as intrinsic alignment (henceforth IA; see Troxel & Ishak 2015; Joachimi et al. 2015; Kiessling et al. 2015; Kirk et al. 2015 for recent reviews): besides carrying information about galaxy formation, intrinsic alignment can impact the cosmological weak lensing effect, namely the change in the path of light, and thus in the observed distribution of galaxies, due to the presence of massive objects along the line of sight. IA must therefore be taken into consideration in deep lensing surveys, such as LSST (LSST Science Collaboration et al. 2009) and Euclid (Laureijs et al. 2011).

Heavens et al. (2000) and Croft & Metzler (2000) first showed the non-negligible contamination of the weak lensing signal due to correlations in the intrinsic shapes of galaxies, and a number of works afterwards (e.g. Heymans et al. 2006; Semboloni et al. 2008) confirmed that this effect must be accounted for in order not to bias the results of the observations.

Measurements of the intrinsic alignment signal have been performed using data from N-body simulations (Heymans et al. 2006; Kuhlen et al. 2007; Lee et al. 2008; Schneider et al. 2012; Joachimi et al. 2013a,b), from hydrodynamical simulations (Codis et al. 2015; Velliscig et al. 2015b; Chisari et al. 2015; Tenneti et al. 2016; Hilbert et al. 2017), and considering observation data as well (Joachimi et al. 2011; Hao et al. 2011; Li et al. 2013; Singh et al. 2015; van Uitert & Joachimi 2017); these two latter groups of data, in particular, claimed that massive red galaxies point towards matter overdensities, while blue galaxies do not show any clear hint of alignment (Hirata et al. 2007; Mandelbaum et al. 2011).

The dependence of the IA signal with mass has also been studied. As far as observations are concerned, the alignment signal is claimed to increase with increasing mass: Hao et al. (2011), for example, studied a large sample of galaxy clusters from the SDSS DR7 finding a dependence of the alignment with the mass of the brightest cluster galaxy, while an increasing trend of the IA amplitude with luminosity, or the corresponding mass, has been

★ E-mail: d.piras@ucl.ac.uk; davide.piras@studenti.unipd.it

identified for galaxies (Joachimi et al. 2011; Singh et al. 2015) and for clusters (van Uitert & Joachimi 2017).

Simulations partially agree with this picture: using a 512^3 -particle N-body simulation, Jing (2002), for example, found that the alignment increases with mass over three orders of magnitude, up to about $10^{13} M_\odot$. Moreover, Lee et al. (2008) used data from the Millennium simulation, and claimed stronger correlations with higher mass over two mass bins around $10^{12} M_\odot$, while Joachimi et al. (2013b), using the same set of data, found an increasing trend over the same mass range only for early-type galaxies, while no dependence on luminosity or particular trend with mass or luminosity for late-type galaxies has been identified.

These results motivate us to search for a universal relation between the alignment strength and the mass of dark matter haloes: first of all, this could lend support to an IA mechanism that successfully explains the trends; moreover, we need to reduce the degrees of freedom in modelling the IA signal, to obtain tighter cosmology constraints from lensing observations. To achieve this, in this work we delve into the dependence of the amplitude of the intrinsic alignment signal on the mass of the halo, which is postulated to drive all the observable properties of the hosted galaxies (e.g. Joachimi et al. 2015): we first derive the expected scaling from the theory, and then test our predictions using data from two N-body simulations, mimicking the observational approach in order to be able to compare our results with real data.

We give details about our theoretical model and derive the expected scaling of the IA with halo mass in the tidal alignment paradigm in Sect. 2; we then present the simulations we work with (Sect. 3.1), and how we define the shapes of the dark matter haloes they contain (Sect. 3.2). In Sect. 4.1 we explain how we measure the correlation between halo shapes, and then (Sect. 4.2) we describe the Bayesian analysis we perform to establish the slope of the power-law model we assume to describe the IA amplitude signal. We finally show our results and compare them with our theoretical predictions (Sect. 5.1) and real data (Sect. 5.2).

2 THEORETICAL BACKGROUND

The physical picture of tidal interaction of a self-gravitating system that is in virial equilibrium with a velocity dispersion σ , such as an elliptical galaxy or a cluster of galaxies, would be a distortion of the system's gravitational potential through tidal gravitational forces. The particles of the system would remain in virial equilibrium and fill up the distorted potential along an isocontour of the gravitational potential, which would result in a change in the shape of the system. This shape should reflect the magnitude and the orientation of the tidal gravitational fields, and the magnitude of the change in shape should depend on how tightly the system is bound.

In isolated virialised systems the Jeans-equation would apply,

$$\frac{1}{\rho} \frac{\partial}{\partial r} \rho(\sigma^2) + \frac{2}{r} \beta_{\text{anis}} \sigma^2 = -\frac{\partial \Phi}{\partial r}, \quad (1)$$

with the particle density ρ , distance r , gravitational potential Φ and the anisotropy parameter β_{anis} , which we set to $\beta_{\text{anis}} = 0$ because we aim to derive only the scaling behaviour of the alignment amplitude. In this case, the Jeans-equation can be solved to yield $\rho \propto \exp(-\Phi/\sigma^2)$.

Gravitational tidal fields generated by the ambient large-scale structure would distort the gravitational potential, and we will work in the limit that the distortion is well-described by a second-order

Taylor-expansion relative to the potential minimum,

$$\Phi \rightarrow \Phi + \frac{1}{2} \frac{\partial^2 \Phi}{\partial r_i \partial r_j} r_i r_j \quad (2)$$

with the distance r_i from the minimum. Consequently, the density of particles would change according to

$$\rho \propto \exp\left(-\frac{\Phi}{\sigma^2}\right) \rightarrow \exp\left(-\frac{\Phi}{\sigma^2}\right) \left(1 + \frac{1}{2\sigma^2} \frac{\partial^2 \Phi}{\partial r_i \partial r_j} r_i r_j\right), \quad (3)$$

and a measurement of the ellipticity through the second moments of ρ would yield a proportionality to $R^2 \partial^2 \Phi / \sigma^2$, with R the size of the object. The expansion is only valid in the limit of weak tidal fields, which is characterised by $R^2 \partial^2 \Phi / \sigma^2 \ll 1$.

Now, the virial relationship $\sigma^2 = GM/R$ sets the velocity dispersion σ^2 into relation with the gravitational potential $-GM/R$, and with the scaling $M \propto R^3$ one would expect $\sigma^2 \propto M^{2/3}$, such that R^2/σ^2 should be constant. Therefore, any scaling of the ellipticity with mass is entirely due to the dependence of tidal gravitational fields with the mass-scale.

The variance of tidal shear fields can be inferred from the variance of the matter density by the Poisson equation, $\Delta \Phi = 3\Omega_m/(2\chi_H^2)\delta$, with the matter density Ω_m and the Hubble-distance $\chi_H = c/H_0$. Computing the tidal shear fields $\partial^2 \Phi$ shows that they must have the same fluctuation statistics as the density field δ . In Fourier-space, the solution to the Poisson equation is $\Phi \propto \delta/k^2$ with the wave vector k , and the tidal shear fields would become $k_i k_j \Phi \propto k_i k_j / k^2 \delta$. Therefore, the spectrum $P_{\partial^2 \Phi}(k)$ of the tidal shear fields is proportional to the spectrum $P_\delta(k)$ of the density fluctuations.

Consequently, one can derive the variance of tidal shear fields from the variance of the density fluctuations, i.e. from the CDM-spectrum $P_\delta(k)$. For doing that, one can relate a mass scale M to the wave vector k by requiring that the mass M should be contained in a sphere of radius R , $M = 4\pi\Omega_m\rho_{\text{crit}}R^3/3$, which in turn defines a scale k in the spectrum which is proportional to $M^{-1/3}$. This implies that on galaxy- and cluster-scales, where the CDM-spectrum scales $\propto k^{-2\dots-3}$, one obtains for the standard deviation of the tidal shear field a behaviour $\propto M^{1/2\dots1/3}$. We compare these very general theoretical predictions with our results in Sect. 5.

3 DATA

3.1 Simulations

In this work we consider haloes from two different simulations:

(i) the **Millennium Simulation (MS)**, first presented in Springel et al. (2005), which uses 2160^3 dark matter particles of mass $m_p^{\text{MS}} = 1.2 \times 10^9 M_\odot$ enclosed in a 500 Mpc/ h -side box. In particular, we consider 2 of its 64 snapshots, i.e. the one at $z = 0$ (snapshot 63), for our baseline, and the one at $z \simeq 0.46$ (snapshot 49), to assess a potential redshift dependence of our findings. Dark matter haloes are identified as in Joachimi et al. (2013a) and references therein: a simple “friends-of-friends” group-finder (FOF, Davis et al. 1985) is run first to spot virialised structures, followed by the SUBFIND algorithm (Springel et al. 2001, 2005) to identify sub-haloes, some of which are then treated as separate haloes if they are only briefly close to the halo. We consider haloes with a minimum number of particles $N_p = 300$.

(ii) The **Millennium-XXL Simulation (MXXL)**, which samples 6720^3 dark matter particles of mass $m_p^{\text{MXXL}} = 8.456 \times 10^9 M_\odot$ confined in a cubic region of 3000 Mpc/ h on a side (Angulo et al.

2012). In this case, we consider only one snapshot, at $z = 0$. Haloes are selected using an ellipsoidal overdensity algorithm, as described in [Despali et al. \(2013\)](#) and [Bonamigo et al. \(2015\)](#): a traditional spherical overdensity algorithm ([Lacey & Cole 1994](#)) gives an initial hint of the true shape and orientation of the halo, which is then improved by building up an ellipsoid using the previously selected particles.

We define the mass of the objects in the catalogues as the mass within a halo which has mean density 200 times the critical value at the redshift corresponding to the respective snapshot (M_{200c}). Note that for the MS we first convert the halo mass from M_{Dhalo} , as defined in [Jiang et al. \(2014\)](#), to M_{200c} using the median line in [Jiang et al. \(2014, figure 2\)](#); this transformation is necessary in order to have a consistent definition of the mass of the haloes in the simulations, but its impact on our results is minimal.

In the simulations the same set of cosmological parameters is adopted, namely they both assume a spatially flat Λ CDM Universe with the total matter density $\Omega_m = \Omega_b + \Omega_{dm} = 0.25$, where $\Omega_b = 0.045$ indicates baryons and $\Omega_{dm} = 0.205$ represents dark matter, a cosmological constant $\Omega_\Lambda = 1 - \Omega_m = 0.75$, the Hubble parameter $h = 0.73$ and the density variance in spheres of radius $8 \text{ Mpc}/h$ $\sigma_8 = 0.9$.

3.2 Halo shapes

We define the simple inertia tensor¹, whose eigenvalues and eigenvectors describe the shape of the halo, as:

$$\mathbf{M}_{\mu\nu} \propto \sum_{i=1}^{N_p} r_{i,\mu} r_{i,\nu}, \quad (4)$$

where N_p is the total number of particles within the halo, and \mathbf{r}_i is the vector that indicates the position of the i -th particle with respect to the centre of the halo, i.e. the location of the gravitational potential minimum. For the MS only, we also consider a reduced inertia tensor, which is defined as ([Pereira et al. 2008](#)):

$$\mathbf{M}_{\mu\nu}^{\text{red}} \propto \sum_{i=1}^{N_p} \frac{r_{i,\mu} r_{i,\nu}}{r_i^2}, \quad (5)$$

with r_i^2 the square of the three-dimensional distance of the i -th particle from the centre of the halo; the reduced inertia tensor is more weighted towards the centre of the halo, and may yield a more reliable approximation of the shape of the galaxy ([Joachimi et al. 2013b](#); [Chisari et al. 2015](#)).

The eigenvectors and eigenvalues define an ellipsoid, which we project onto one of the faces of the simulation box: the resulting ellipse is the projected shape of the halo. We proceed as in [Joachimi et al. \(2013b\)](#) to define the ellipticity ϵ of the objects, adopting their procedure for early-type galaxies. We indicate the three unit eigenvectors as $\mathbf{s}_\mu = \{s_{x,\mu}, s_{y,\mu}, s_{\parallel,\mu}\}^\top$ and the absolute values of the semi-axes as $\omega_\mu, \mu \in \{1, 2, 3\}$, with which we define a symmetric tensor

$$\mathbf{W}^{-1} = \sum_{\mu=1}^3 \frac{s_{\perp,\mu} s_{\perp,\mu}^\top}{\omega_\mu^2} - \frac{\kappa \kappa^\top}{\alpha^2}, \quad (6)$$

¹ MS and MXXL use two different tensor definitions to describe the shape, but they result in the same halo ellipticity (see also [Bett et al. 2007](#) for further details).

with $s_{\perp,\mu} = \{s_{x,\mu}, s_{y,\mu}\}^\top$ the eigenvector projected along the line of sight,

$$\kappa = \sum_{\mu=1}^3 \frac{s_{\parallel,\mu} s_{\perp,\mu}}{\omega_\mu^2}, \quad (7)$$

and

$$\alpha^2 = \sum_{\mu=1}^3 \left(\frac{s_{\parallel,\mu}}{\omega_\mu} \right)^2. \quad (8)$$

We compute the two Cartesian components of the ellipticity ([Bartelmann & Schneider 2001](#))

$$\epsilon_1 = \frac{W_{11} - W_{22}}{W_{11} + W_{22} + 2\sqrt{\det \mathbf{W}}}, \quad (9)$$

$$\epsilon_2 = \frac{2W_{12}}{W_{11} + W_{22} + 2\sqrt{\det \mathbf{W}}}, \quad (10)$$

which we then translate in the tangential (+) component, following the IA sign convention²:

$$\epsilon_+ = \epsilon_1 \cos(2\varphi) + \epsilon_2 \sin(2\varphi), \quad (11)$$

where φ is the polar angle of the line that connects haloes pair, in the reference frame of the simulation box. We show how we use ϵ_+ to measure the correlation between halo shapes in the next section.

4 METHODOLOGY

4.1 Measurements

To measure the alignment of every dark matter halo with other haloes, which we use as tracers of the density field, we mimic the standard analysis that is usually performed with observation data (e.g. [van Uitert & Joachimi 2017](#)), i.e. we use biased tracers and the same statistic. Instead of fitting complicated models to the alignment signal and dividing out the galaxy/cluster bias dependence afterwards, though, we choose one large bin in the comoving transverse distance R_p , and proceed as follows to dispose of the bias factor.

We first define an estimator as a function of R_p and the line-of-sight distance Π :

$$\hat{\xi}_{g+}(R_p, \Pi) = \frac{S_+ D}{DD}, \quad (12)$$

where $S_+ D$ represents the correlation between cluster shapes and the density sample (ϵ_+), and DD the number of cluster shape-density pairs. We then integrate along the line of sight to obtain the total projected intrinsic alignment signal:

$$\hat{w}_{g+}(R_p) = \int_{-\Pi_{\max}}^{\Pi_{\max}} d\Pi \hat{\xi}_{g+}(R_p, \Pi). \quad (13)$$

Throughout this work, we adopt $\Pi_{\max} = 60 \text{ Mpc}/h$, a value large enough not to miss part of the signal, but small enough not to pick up too much noise. We describe the intrinsic alignment signal by simplifying the model in [van Uitert & Joachimi \(2017, equation 5\)](#), namely we assume:

$$w_{g+}(R_p, M) = A_{\text{IA}}(M) b_g(M) w_{\delta+}^{\text{model}}(R_p), \quad (14)$$

with $A_{\text{IA}}(M)$ the amplitude of the intrinsic alignment signal, $b_g(M)$

² Our definition of ϵ_+ has an opposite sign with respect to, for example, [Bartelmann & Schneider \(2001\)](#), as commonly adopted in IA works.

the cluster bias and $w_{\delta+}^{\text{model}}(R_p)$ a function in which we include the dependence on R_p . In the tidal alignment paradigm, $w_{\delta+}^{\text{model}}$ is independent of the halo mass, since it is fully determined by the properties of the dark matter distribution, assuming that any mass dependence of the response of a halo shape to the tidal gravitational field is captured by A_{IA} .

We evaluate the expression in Eq. 14 in the interval which covers $6 \text{ Mpc}/h < R_p < 30 \text{ Mpc}/h$, denoted by R_p^* , to get rid of the dependence on R_p ; in other words, we define:

$$w_{g+}(M) \equiv w_{g+}(R_p = R_p^*, M). \quad (15)$$

We choose this particular interval for many reasons: to begin with, $6 \text{ Mpc}/h$ is the lower endpoint usually adopted in observational papers; also, below this threshold the bias becomes non-linear (Joachimi et al. 2013b). Finally, only noise is added to the signal above $30 \text{ Mpc}/h$.

We use the LS (Landy & Szalay 1993) estimator to calculate the clustering signal:

$$\hat{\xi}_{\text{gg}}(R_p, \Pi) = \frac{DD - 2DR + RR}{RR}, \quad (16)$$

where DD represents the number of cluster pairs, DR the number of cluster-random point pairs, and RR the number of random point pairs. To measure DR and RR , we generate random catalogues that contain objects uniformly distributed between the minimum and maximum value of the x , y and z coordinates of each sub-box³. These catalogues normally are 3 times denser; in some cases, when a sub-box encloses very few objects, we switch to random catalogues which are 10 times denser. We then integrate along the line of sight to obtain the total projected clustering signal:

$$\hat{w}_{\text{gg}}(R_p) = \int_{-\Pi_{\text{max}}}^{\Pi_{\text{max}}} d\Pi \hat{\xi}_{\text{gg}}(R_p, \Pi). \quad (17)$$

We describe the clustering signal with a simple model:

$$w_{\text{gg}}(R_p, M) = b_g^2(M) w_{\delta\delta}^{\text{model}}(R_p) - C_{\text{IC}}, \quad (18)$$

with $w_{\delta\delta}^{\text{model}}(R_p)$ a function in which we include the dependence on R_p (van Uitert & Joachimi 2017, equation 9), and C_{IC} the integral constraint, which we estimate as in Roche & Eales (1999, equation 8) using the random pair counts. Note that, since we are dealing with dark matter clustering, $w_{\delta\delta}^{\text{model}}(R_p)$ does not depend on the mass of the halo. Again, we evaluate the previous expression in R_p^* , obtaining:

$$w_{\text{gg}}(M) \equiv w_{\text{gg}}(R_p = R_p^*, M). \quad (19)$$

In observational analyses, the bias factor is usually held fixed to a precise value; equivalently, to remove the mass dependence of the halo bias $b_g(M)$, we define:

$$r_{g+}(M) = \frac{w_{g+}(M)}{\sqrt{w_{\text{gg}}(M)}} = \frac{A_{\text{IA}}(M) w_{\delta+}^{\text{model}}(R_p = R_p^*)}{\sqrt{w_{\delta\delta}^{\text{model}}(R_p = R_p^*)}} \propto A_{\text{IA}}(M), \quad (20)$$

where we assume that the clustering signal $w_{\text{gg}}(M)$ is positive (see Sect. 4.2 and Sect. 5 for further discussion). We stress that, under our assumptions, this quantity depends only on the mass of the halo M .

³ For further information about the sub-boxes, see Sect. 4.2.

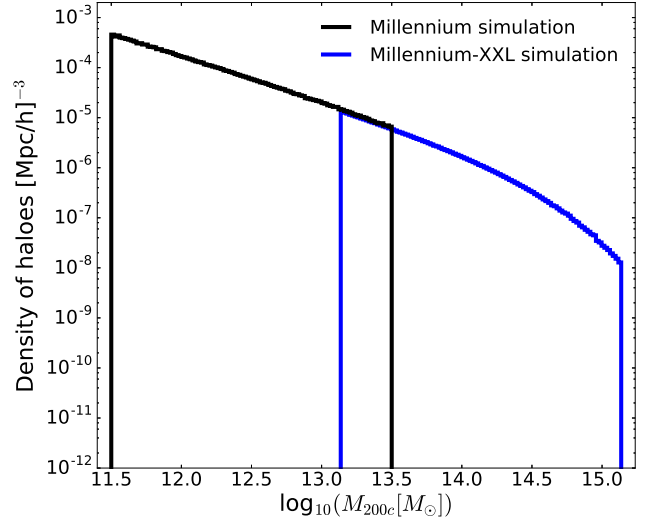


Figure 1. Histogram showing the density distribution of the mass of the haloes. In this case, the mass of the halo is defined considering an overdensity of 200 times the critical value (M_{200c}), as explained in Sect. 3.1. In the range where the selected bins overlap, the trend of the density agrees for the two simulations.

4.2 Modelling

The goal of this paper is to study the dependence on the mass of the amplitude $A_{\text{IA}}(M)$ by studying the quantity $r_{g+}(M)$. We adopt the following model for $r_{g+}(M)$:

$$r_{g+}(M) = A \cdot \left(\frac{M}{M_p} \right)^{\beta_M}, \quad (21)$$

with A a generic amplitude which we will treat as a nuisance parameter, $M_p = 10^{13.5} M_\odot / h_{70}$ a pivot mass, and β_M a free power-law index, which we intend to compare with the value predicted in Sect. 2.

To achieve this goal, we select the haloes from the catalogues described in Sect. 3.1 in $n = 4$ logarithmic mass bins, between $10^{11.5} M_\odot$ and $10^{13.5} M_\odot$ for the MS and between $10^{13} M_\odot/h$ and $10^{15} M_\odot/h$ for the MXXL, we split them in $N = 3^3 = 27$ sub-boxes based on their positions inside the cube of the respective simulation, and calculate w_{g+} and w_{gg} for each of the N sub-samples by replacing the integrals in Eq. 13 and 17 with a sum over 20 line-of-sight bins, each $2\Pi_{\text{max}}/20 = 6 \text{ Mpc}/h$ wide. We define the line of sight as the projection of the distance of the objects along the z axis. We show the density distribution of the selected masses for the two catalogues in Fig. 1.

We then perform a likelihood analysis over the data to infer the posteriors of A and β_M : according to Bayes' theorem, if \mathbf{d} is the vector of the data and \mathbf{p} the vector of the parameters,

$$P(\mathbf{p}|\mathbf{d}) \propto P(\mathbf{d}|\mathbf{p}) P(\mathbf{p}) \propto e^{-\frac{1}{2}\chi^2} P(\mathbf{p}), \quad (22)$$

with $P(\mathbf{p}|\mathbf{d})$ the posterior probability, $P(\mathbf{d}|\mathbf{p})$ the likelihood function, $P(\mathbf{p})$ the prior probability and $\chi^2 = (\mathbf{d} - \mathbf{m})^T \mathbf{C}^{-1} (\mathbf{d} - \mathbf{m})$, with \mathbf{m} the vector of the model and \mathbf{C}^{-1} the precision matrix, the inverse of the covariance matrix \mathbf{C} . We assume uninformative flat priors in the fit with ranges $\log_{10} A \in [-1.9; -0.4]$ and $\beta_M \in [-0.3; 0.7]$.

We estimate the covariance matrix from the data:

$$\mathbf{C}_{\mu\nu} = \frac{1}{N-1} \sum_{j=1}^N (d_{j,\mu} - \bar{d}_\mu)(d_{j,\nu} - \bar{d}_\nu), \quad (23)$$

with $\mu, \nu \in \{1, \dots, n\}$, $\bar{d}_\mu = \frac{1}{N} \sum_{j=1}^N d_{j,\mu}$, and $d_{j,\mu} = r_{g+}(M)$ for each sub-box and each mass bin, as defined in Eq. 20. We then invert the covariance matrix and correct the bias on the inverse to obtain an unbiased estimate of the precision matrix, given by:

$$\mathbf{C}_{\text{unbiased}}^{-1} = \frac{N - n - 2}{N - 1} \mathbf{C}^{-1}, \quad (24)$$

where $N > n + 2$ clearly holds (Taylor et al. 2013). The results of the analysis are presented in Sect. 5.

The choice of n and N is constrained by many factors: first of all, if N is too large, the single values of w_{gg} (and w_{g+}) tend to fluctuate around the mean, thus increasing the error bar and sometimes plunging below 0, which is unacceptable for our choice of $r_{g+}(M)$; see Eq. 20. Furthermore, we want n to be large enough to be capable of displaying the trend of the signals along the whole mass range chosen. Finally, we need to take $n \ll N$ to avoid divergences related to the fact that we estimate the covariance from a finite number of samples (Taylor et al. 2013).

5 RESULTS AND DISCUSSION

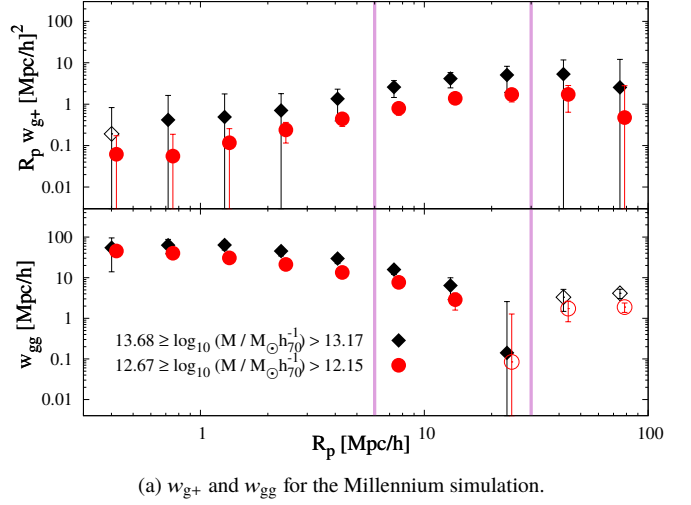
5.1 Simulation data

To be able to compare our results with those in van Uitert & Joachimi (2017, figure 7) we convert our M_{200c} to M_{200m} , defined as the mass within a halo which has mean density 200 times the mean background value at the redshift corresponding to the respective snapshot.

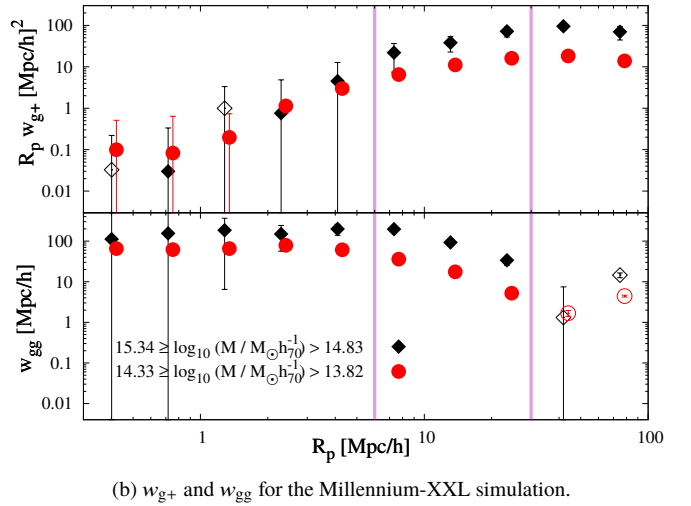
The trend of w_{g+} and w_{gg} with R_p for 2 of the 4 mass bins for both the catalogues is shown in Fig. 2. Note that even though in the chosen interval w_{gg} is not always positive within the error bar, our choice of n and N and our large-bin average ensure that Eq. 20 always returns a real value. The points shown in Fig. 2 are the arithmetic mean of the N values for each mass bin, while the error bars are the standard deviation of the values. The overall behaviour of w_{g+} and w_{gg} agrees with previous works (Joachimi et al. 2011; van Uitert & Joachimi 2017); in particular, we clearly detect positive intrinsic alignment in all samples, implying that dark matter haloes tend to point towards the position of other haloes. Also, it is worth noting that both signals increase with increasing mass.

We then study the dependence of w_{g+} , w_{gg} and r_{g+} on the mass of the halo. In Fig. 3 we also include, for the Millennium simulation only, two more results: grey dots represent the signal from the objects at redshift $z = 0.46$, while open black dots represent the signal from the objects at $z = 0$ obtained using the reduced inertia tensor (*rit*, as in Eq. 5), instead of the simple one, to measure the shapes of the haloes. As one can see, despite the use of two different halo finders and two different quantities to measure the shapes, as mentioned in Sect. 3.1 and in Sect. 3.2, respectively, the MS and the MXXL follow the same trend, and yield consistent results in the small mass range where they overlap; furthermore, all three w_{g+} , w_{gg} and r_{g+} increase with increasing mass. As a side note, we mention that the *rit* leads to lower alignment signals, as found in Joachimi et al. (2013b), and that, on the other hand, these signals increase with increasing redshift.

We proceed by showing the results of the likelihood analysis described in Sect. 4.2: Fig. 4(a) shows the results from the single catalogues and from the joint analysis of the two simulations, obtained by multiplying the likelihood functions and assuming the same flat priors on the parameters. The most stringent bounds come from the M-XXL simulation, while the MS yields larger errors on the parameters, albeit consistent with the results of the MXXL. The joint



(a) w_{g+} and w_{gg} for the Millennium simulation.



(b) w_{g+} and w_{gg} for the Millennium-XXL simulation.

Figure 2. Trend of the intrinsic alignment signal w_{g+} and the cluster signal w_{gg} with the comoving transverse distance R_p for (a) the Millennium and (b) the Millennium-XXL simulation. The pink lines indicate the $6 < R_p / \text{Mpc}/h < 30$ interval. The mass ranges are displayed considering M_{200m} as the mass of the halo, and correspond to the second and the fourth bin of our division, explained in detail in Sect. 4.2. In the graph, points are slightly horizontally shifted, so that they do not overlap; negative values are displayed in absolute value with open symbols of the same colour. An increasing trend with mass is clear in each panel separately, and comparing the two panels as well.

analysis returns a value for the slope compatible with $\beta_M = 1/3$, which agrees remarkably well with the predictions made in Sect. 2 for a DM-only Universe; in particular, the tightest constraints are obtained with cluster-size objects (0.5 Mpc–1.5 Mpc), where the non-linear matter power spectrum is proportional to $k^{-2.2}$ (Blas et al. 2011), yielding $\beta_M \simeq 0.37$, excellently compatible with our high-mass results. Moreover, we find that neither the inertia tensor definition nor the chosen redshift for our default analysis have significant impact on our conclusions for β_M . We report all the best-fit values, together with their respective errors and reduced χ^2 , in Table 1.

The very low reduced χ^2 value of the MS can be attributed to the fact that all the points lie along the best-fit line, while we note that the high value of the MXXL can be lowered to 0.82 by excluding the highest-mass point: in this last bin, we probably underestimate

Table 1. Results of the likelihood analysis over the Millennium simulation, the Millennium-XXL simulation, their joint contribution, the Millennium simulation at $z = 0.46$, the Millennium simulation using the reduced inertia tensor and real data. Note that the values from the snapshot at different redshift and from the reduced inertia tensor assumption are compatible with the outcomes of the MS only. A discussion about the reasons why the reduced χ^2 values obtained considering the two simulations separately and real data significantly differ from 1 is present in the text.

	MS only	MXXL only	Joint	MS, $z = 0.46$	MS, rit
β_M	$0.29^{+0.14}_{-0.16}$	$0.36^{+0.03}_{-0.03}$	$0.35^{+0.03}_{-0.03}$	$0.34^{+0.12}_{-0.17}$	$0.29^{+0.13}_{-0.15}$
$\log_{10}(A \text{ [Mpc/h]}^{1/2})$	$-0.85^{+0.17}_{-0.26}$	$-0.82^{+0.01}_{-0.02}$	$-0.82^{+0.01}_{-0.01}$	$-0.59^{+0.17}_{-0.26}$	$-1.07^{+0.17}_{-0.25}$
χ^2/dof	0.03	1.60	0.62	0.05	0.01
Real data					
β_M	$0.56^{+0.05}_{-0.05}$				
$\log_{10} A_r$	$0.61^{+0.03}_{-0.04}$				
χ^2/dof	1.68				

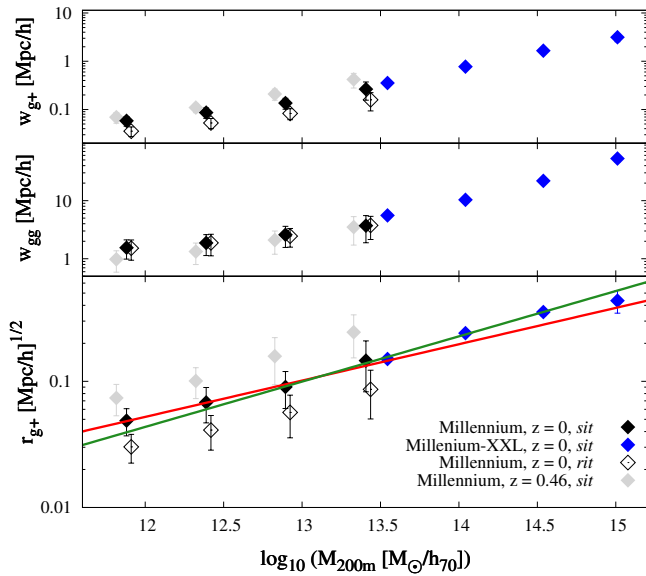


Figure 3. Trend of the intrinsic alignment signal w_{g+} , the cluster signal w_{gg} and r_{g+} as defined in Eq. 20 with the halo mass M_{200m} for the Millennium and the Millennium-XXL simulations. The label *sit* stands for simple inertia tensor, while *rit* means reduced inertia tensor; note that for the MXXL data only the simple inertia tensor is available, as mentioned in Sect. 3.2. The points are not placed at the midpoint of the bin, but at the value corresponding to the arithmetic mean of the mass of the objects. The red and green lines represent the best-fit line for the MS and MXXL likelihood analyses respectively; they are drawn using the parameters reported in Table 1. Points showing the results from the *rit* choice are horizontally shifted by a small amount, so that they do not overlap with the corresponding *sit* dots.

the error on the data point, since we deal with a very little number of objects, many less than in the other bins, as one can see from Fig. 1.

5.2 Observation data

To compare our results with real data, we also take into consideration the analysis presented in van Uitert & Joachimi (2017): in that work, the clusters contained in the redMaPPer catalogue (Rykoff et al. 2014) version 6.3 were used to constrain the intrinsic alignment signal amplitude A_{IA} , which was then studied as a function of the halo mass.

We repeat the likelihood analysis for the collection of obser-

vational datasets used in van Uitert & Joachimi (2017, figure 7): we consider all 21 data points, neglect the error bars on the mass, which are smaller than the errors on A_{IA} and whose negligible impact is studied in van Uitert & Joachimi, and treat all the data as independent, so that the covariance matrix is diagonal. This latter assumption is safe, since the data all have used different approaches to estimate their errors, and thus the noise impact, besides being hard to model, can be neglected. We show the points, together with the best-fit line from our analysis, in Fig. 5.

In this case, we need to slightly change the model in Eq. 21, since we are dealing with a different quantity. We assume the same power-law model with a different prefactor A_r , which has an altered meaning and is now dimensionless, thus making it impossible to directly compare its value to the one that is suggested by the simulation data. We also assume a different range regarding the flat prior in the fit for this new parameter, namely $\log_{10} A_r \in [0.4; 0.9]$.

The outcomes of our analysis are shown in Fig. 4(b) and in Table 1: we observe that the value of the reduced chi-square for this latter analysis is not as good as in the joint analysis with the simulated data, but can be improved to 1.36 by excluding the high-redshift SDSS results (filled-blue diamonds) without affecting the value of the slope in a significant way.

While the disagreement between the values of the prefactor can be easily justified, since we are using different definitions of the amplitude of the intrinsic alignment signal, the incompatibility between the values of the slope β_M between simulation and real data is significant, and can be attributed to the fact that, while we observe bright matter, the simulations and the theory model only consider dark matter. A more detailed discussion about the reasons that could explain the discrepancy is presented in the next section.

6 CONCLUSIONS

In this work we studied the dependence of the intrinsic alignment amplitude on the mass of dark matter haloes, using data from the Millennium and Millennium-XXL N-body simulations.

We derived the intrinsic alignment scaling with mass in the tidal alignment paradigm for a dark matter-only Universe, and predicted that it follows a power law with slope $\beta_M = 1/2 \dots 1/3$. We mimicked the observational approach to measure the halo shape-position alignments, and performed a Bayesian analysis on our data to test the theoretical forecast. We found that simulation data agree remarkably well with each other and, more noticeably, with $\beta_M = 1/3$; in particular, the joint analysis yields $\beta_M = 0.35^{+0.03}_{-0.03}$.

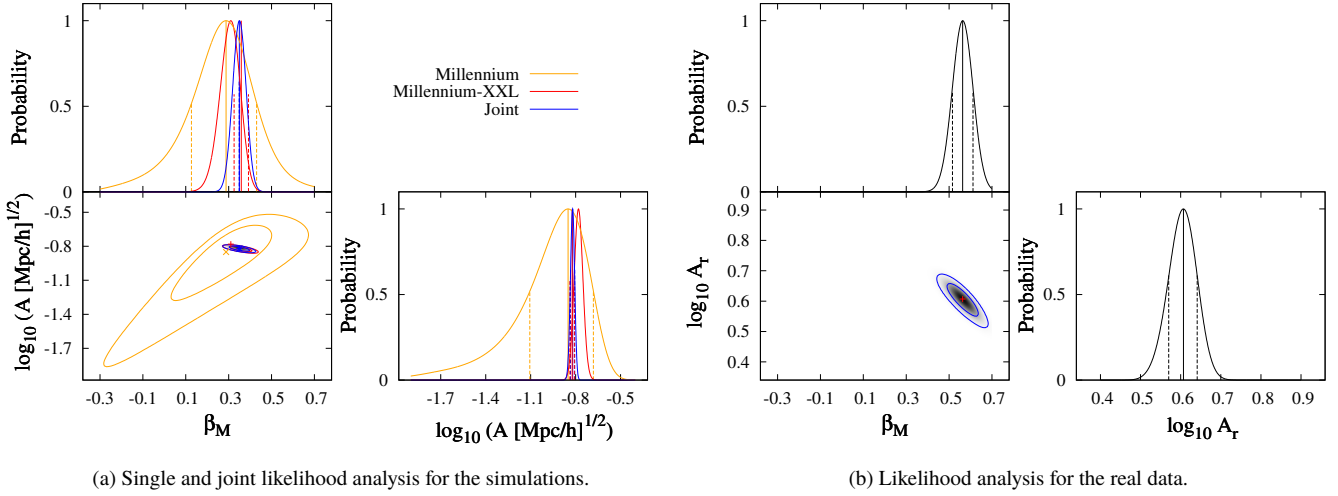


Figure 4. Likelihood analysis for (a) the Millennium simulation, the M-XXL simulation, joint MS and MXXL, and (b) real data; note that, while the same range for β_M is assumed, the ranges of the prefactors are quite different. The bottom-left graph in the right panel shows the 2-D posterior for the real data, while the bottom-left graph in the left panel shows the contour lines of the 2-D posteriors for all the simulations (single and joint), but the 2-D posterior for the joint analysis only. All other sub-panels show the marginalized 1-D posterior normalized to a peak amplitude of 1. Contour lines enclose the 68% and 95% confidence intervals, dots and vertical solid lines indicate the best-fitting values, while dashed lines represent the $1-\sigma$ confidence interval. We note that the MS returns larger error bars, but the results are consistent for the two catalogues, while real data yield a value of the slope which is incompatible with the one from the joint analysis. The exact values and errors of A , A_r and β_M are presented in Table 1.

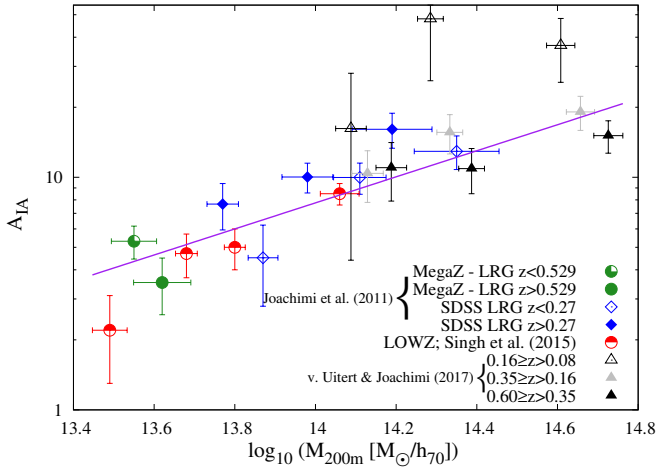


Figure 5. Real data, as shown in van Uitert & Joachimi (2017, figure 7), with the best-fit line from our likelihood analysis. The exact values of the parameters are shown in Table 1.

Furthermore, there is no dependence of these results on redshift or on the definition of the inertia tensor which describes the shape of the halo.

We repeated our statistical analysis using observational data, inferring a value of $\beta_M = 0.56^{+0.05}_{-0.05}$, which is not compatible with the simulation results. The discrepancy can be attributed to the fact that simulations consider a dark-matter only Universe, while we observe luminous matter. A possible future work in this sense would be then to test the slope β_M using a hydrodynamical simulation large enough to contain clusters, which could then account for the additional effects of baryons and gas.

We finally point out that the presence of baryons could significantly affect the shape of the host dark matter halo, especially in the inner regions, as hydrodynamical simulations suggest (Kießling

et al. 2015, and references therein). For example, Bailin et al. (2005) found an increasing halo sphericity decreasing with increasing radius (and thus with increasing mass), in agreement with Kazantzidis et al. (2004), while more recently Tenneti et al. (2014) and Velliscig et al. (2015a) discovered that galaxies are more misaligned with the hosting halo at lower masses.

All these papers suggest that it is safe to assume that galaxies and clusters of galaxies are less aligned with each other than haloes at lower mass values, which means that the slope β_M expected from the observation data should be higher than in the case of a dark matter-only scenario, in agreement with what we found in this work.

ACKNOWLEDGEMENTS

REFERENCES

- Angulo R. E., Springel V., White S. D. M., Jenkins A., Baugh C. M., Frenk C. S., 2012, *MNRAS*, **426**, 2046
- Bailin J., et al., 2005, *ApJ*, **627**, L17
- Bartelmann M., Schneider P., 2001, *Phys. Rep.*, **340**, 291
- Bett P., Eke V., Frenk C. S., Jenkins A., Helly J., Navarro J., 2007, *MNRAS*, **376**, 215
- Blas D., Lesgourgues J., Tram T., 2011, *J. Cosmology Astropart. Phys.*, **7**, 034
- Bonamigo M., Despali G., Limousin M., Angulo R., Giocoli C., Soucail G., 2015, *MNRAS*, **449**, 3171
- Chisari N., et al., 2015, *MNRAS*, **454**, 2736
- Codis S., et al., 2015, *MNRAS*, **448**, 3391
- Croft R. A. C., Metzler C. A., 2000, *ApJ*, **545**, 561
- Davis M., Efstathiou G., Frenk C. S., White S. D. M., 1985, *ApJ*, **292**, 371
- Despali G., Tormen G., Sheth R. K., 2013, *MNRAS*, **431**, 1143
- Hao J., Kubo J. M., Feldmann R., Annis J., Johnston D. E., Lin H., McKay T. A., 2011, *ApJ*, **740**, 39
- Heavens A., Refregier A., Heymans C., 2000, *MNRAS*, **319**, 649

- Heymans C., White M., Heavens A., Vale C., Van Waerbeke L., 2006, *MNRAS*, **371**, 750
- Hilbert S., Xu D., Schneider P., Springel V., Vogelsberger M., Hernquist L., 2017, *MNRAS*, **468**, 790
- Hirata C. M., Mandelbaum R., Ishak M., Seljak U., Nichol R., Pimbblet K. A., Ross N. P., Wake D., 2007, *MNRAS*, **381**, 1197
- Jiang L., Helly J. C., Cole S., Frenk C. S., 2014, *MNRAS*, **440**, 2115
- Jing Y. P., 2002, *MNRAS*, **335**, L89
- Joachimi B., Mandelbaum R., Abdalla F. B., Bridle S. L., 2011, *A&A*, **527**, A26
- Joachimi B., Semboloni E., Bett P. E., Hartlap J., Hilbert S., Hoekstra H., Schneider P., Schrabback T., 2013a, *MNRAS*, **431**, 477
- Joachimi B., Semboloni E., Hilbert S., Bett P. E., Hartlap J., Hoekstra H., Schneider P., 2013b, *MNRAS*, **436**, 819
- Joachimi B., et al., 2015, *Space Sci. Rev.*, **193**, 1
- Kazantzidis S., Kravtsov A. V., Zentner A. R., Allgood B., Nagai D., Moore B., 2004, *ApJ*, **611**, L73
- Kiessling A., et al., 2015, *Space Sci. Rev.*, **193**, 67
- Kirk D., et al., 2015, *Space Sci. Rev.*, **193**, 139
- Kuhlen M., Diemand J., Madau P., 2007, *ApJ*, **671**, 1135
- LSST Science Collaboration et al., 2009, preprint, ([arXiv:0912.0201](https://arxiv.org/abs/0912.0201))
- Lacey C., Cole S., 1994, *MNRAS*, **271**, 676
- Landy S. D., Szalay A. S., 1993, *ApJ*, **412**, 64
- Laureijs R., et al., 2011, preprint, ([arXiv:1110.3193](https://arxiv.org/abs/1110.3193))
- Lee J., Springel V., Pen U.-L., Lemson G., 2008, *MNRAS*, **389**, 1266
- Li C., Jing Y. P., Faltenbacher A., Wang J., 2013, *ApJ*, **770**, L12
- Mandelbaum R., et al., 2011, *MNRAS*, **410**, 844
- Pereira M. J., Bryan G. L., Gill S. P. D., 2008, *ApJ*, **672**, 825
- Roche N., Eales S. A., 1999, *MNRAS*, **307**, 703
- Rykoff E. S., et al., 2014, *ApJ*, **785**, 104
- Schneider M. D., Frenk C. S., Cole S., 2012, *J. Cosmology Astropart. Phys.*, **5**, 030
- Semboloni E., Heymans C., van Waerbeke L., Schneider P., 2008, *MNRAS*, **388**, 991
- Singh S., Mandelbaum R., More S., 2015, *MNRAS*, **450**, 2195
- Springel V., White S. D. M., Tormen G., Kauffmann G., 2001, *MNRAS*, **328**, 726
- Springel V., et al., 2005, *Nature*, **435**, 629
- Taylor A., Joachimi B., Kitching T., 2013, *MNRAS*, **432**, 1928
- Tenneti A., Mandelbaum R., Di Matteo T., Feng Y., Khandai N., 2014, *MNRAS*, **441**, 470
- Tenneti A., Mandelbaum R., Di Matteo T., 2016, *MNRAS*, **462**, 2668
- Troxel M. A., Ishak M., 2015, *Phys. Rep.*, **558**, 1
- Velliscig M., et al., 2015a, *MNRAS*, **453**, 721
- Velliscig M., et al., 2015b, *MNRAS*, **454**, 3328
- van Uitert E., Joachimi B., 2017, preprint, ([arXiv:1701.02307](https://arxiv.org/abs/1701.02307))

This paper has been typeset from a \LaTeX file prepared by the author.